The shape and behaviour of a granular bed in a rotating drum using Eulerian flow fields obtained from PEPT

Morrison, A.j.; Govender, I.; Mainza, A.n.; Parker, David

DOI:
10.1016/j.ces.2016.06.022

The shape and behaviour of a granular bed in a rotating drum using Eulerian flow fields obtained from PEPT

A.J. Morrison, I. Govender, A.N. Mainza, D.J. Parker

Chemical Engineering Science

www.elsevier.com/locate/ces

PII: S0009-2509(16)30318-9
DOI: http://dx.doi.org/10.1016/j.ces.2016.06.022
Reference: CES13002

To appear in: *Chemical Engineering Science*

Received date: 29 January 2016
Revised date: 2 June 2016
Accepted date: 9 June 2016

The shape and behaviour of a granular bed in a rotating drum using Eulerian flow fields obtained from PEPT

A. J. Morrison[b], I. Govender[a,b,*], A. N. Mainza[b], D. J. Parker[c]

[a]*School of Engineering, University of KwaZulu-Natal, Glenwood, 4041*

[b]*Centre for Minerals Research, University of Cape Town, P/Bag Rondebosch, 7701*

[c]*School of Physics and Astronomy, University of Birmingham, Edgbaston, Birmingham B15 2TT, UK*

Abstract

Non-invasive single-particle tracking techniques, such as positron emission particle tracking (PEPT), provide useful information about the behaviour of a representative particle moving in a bulk of similar particles in a rotating drum. The Lagrangian trajectories that they yield can be used to study, for example, particulate diffusion or granular interaction. However, often the Eulerian flow fields of the entire granular bed are more useful– they can be used to study segregation, for instance, or the evolution of the free surface of the bed. In this work, we present a technique for converting Lagrangian trajectories to Eulerian flow fields via a time-weighted residence time distribution (RTD) of the tracked particle. We then perform PEPT experiments on a mono-disperse bed of spherical particles in a cylindrical drum, rotated at various rates, and use the RTD procedure to obtain flow fields of the bed. We use these flow fields to investigate the effect of drum rotational speed on the shape and behaviour of a granular bed in a rotating drum, and the insights gained thereby to define a comprehensive set of surfaces– such as the bulk free surface– to divide the bed into regions of distinct granular behaviour. We further define scalar bed features– such as the centre of circulation of the bed– that can be used to quantitatively compare the behaviour of granular beds in rotating drums operated under various conditions.

Keywords: PEPT, positron emission particle tracking, granular flow, rotating drums, free surfaces, residence time distribution, RTD

*Corresponding author
Email address: indresan.govender@gmail.com (I. Govender)

Introduction

A bed of granular material in a rotating drum can experience a wide range of phenomena– from perfect mixing to convection and size segregation– depending on the conditions under which the drum is operated. The types of behaviour that such a granular bed can exhibit have been classified into various categories by Boateng and Barr (1996), Mellmann (2001) and Ding et al. (2002). These categories, or modes, are collected and summarised in figure 1.

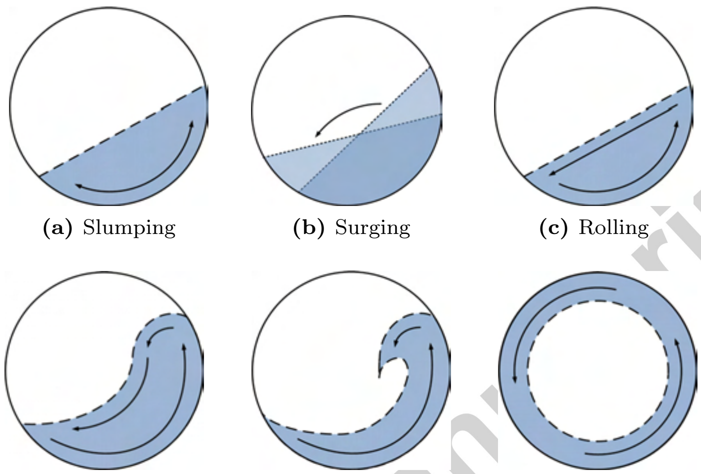

(a) Slumping **(b)** Surging **(c)** Rolling

(d) Cascading **(e)** Cataracting **(f)** Centrifuging

Figure 1: Six categories of granular bed motion in a rotating drum in order of increasing rotational speed, left to right and top to bottom.

These behaviours are exploited industrially in a range of material-handling applications, including powder mixers, rotary kilns, trommels, and grinding mills. Of most interest for all of these applications are the cascading and cataracting modes, which will be the focus of this paper. Which of these modes obtains in a rotating drum is most determined by two operating variables: the drum's rotational speed, and the fraction of its volume occupied by the granular material.

For ease of comparison across drum sizes, rotational speed can be expressed as a fraction of critical speed, N_C, which is the rotational speed at which the outermost layer of granular material in a rotating drum begins to centrifuge. It is defined by Rose and Sullivan (1957), in revolutions per second, as:

$$N_c = \frac{1}{2\pi}\sqrt{\frac{2g}{D-2r}} \tag{1}$$

where D is the inner diameter of the rotating drum, g is the acceleration due to gravity, and r is the radius of a representative grain in the bed. Many industrial rotating drums satisfy the additional condition that $r << D$, which allows the critical speed to be expressed more simply, in revolutions per minute, as:

$$N_c \approx \frac{42.3}{\sqrt{D}}. \tag{2}$$

Although equation 2 is an imperfect approximation, even for mono-disperse granular materials, and although the critical speed of a rotating drum has been shown to be more complicated than that shown in equation 1 (Watanabe, 1999), we employ the definition in equation 2 for ease of comparison with industry and industrial data.

Also for comparison with industrial data, the volume of granular material in the drum is not expressed as a volume fraction, but as a load fraction, f. The load is that volume of material that would completely fill the drum. Thus the load fraction differs from the volume fraction by a factor of the packing fraction, η. The load fraction can be expressed as:

$$f = \frac{V_m}{\eta V_d} \tag{3}$$

where V_m is the volume of the granular material, and V_d the internal volume of the drum. Defining the load fraction in this way has the effect that the occupied fraction of the drum can increase as the dynamic granular bed dilates, and thus the bed packing fraction decreases.

Due to the breadth of applications of rotating drums in granular handling operations, knowing how the behaviour of a granular bed will change in response to varying operating conditions, such as drum rotational speed and filling, is of significant interest to industry. This work will go some way towards providing an unambiguous means of characterising the type of motion undergone by a granular bed from either Lagrangian or Eulerian experimental data.

The rest of the paper is organised as follows: first, various sources of the necessary experimental data are discussed generally, and the technique employed here, positron emission particle tracking (PEPT), in detail. Next, a means of interpreting such Lagrangian trajectory data as a Eulerian probability and kinematic fields is introduced. Numerical schemes are then presented to characterise and delineate various features and regions of a dynamic granular bed undergoing cascading and cataracting motion in a rotating drum. Finally, these numerical schemes are used to compare the shape and behaviour of the granular bed in a rotating drum operated at three different rotational speeds, using data obtained with the PEPT technique.

The experimental study of granular motion in rotating drums

Various experimental techniques have been used to study granular flows in rotating drums, predominantly in the context of rotary kilns and of tumbling mills. These techniques can be divided into two categories– visual and radiological.

The visual experiments generally consist of a laboratory-scale rotating drum fitted with a transparent end window through which the dynamic granular bed is observed. The dynamic bed is then either filmed to obtain a dynamic picture of the motion of the bed, or photographed. Such techniques were used by, for instance Rogovin and Herbst (1989), Morrell (1992), Santomaso et al. (2003) and Tordesillas and Arber (2005). Another well-developed method is Particle Image Velocimetry (PIV), which involves comparing the positions of tracer particles in sequences of high-speed photographs (Jain et al., 2002).

The obvious drawback of end-window techniques is that they are limited to what can be seen through the side of the drum. This makes it impossible to control for obfuscating end effects that may not be representative of the motion of the bulk of the charge. To overcome this limitation, radiological techniques were developed to image the bulk behaviour of a granular bed. Nakagawa et al. (1993), for instance, used nuclear magnetic resonance imaging (NMRI) to study the motion of mustard seeds in a rotary kiln. Similarly, Powell and Nurick (1996b) used biplanar x-ray imaging of a rotating drum to obtain, by the density-dependent transmission of x-rays through matter, a better representation of the shape of the dynamic bed in the drum. Govender et al. (2001) extended this technique to single-particle tracking of a more-attenuating particle in a bulk of similar particles as a means of obtaining a more representative velocity of the tracer particle in the bulk.

Subsequently, PEPT has also been successfully used to non-invasively recover the Lagrangian trajectories of a radio-labelled particle in rotating drums by Ding et al. (2001a), Ding et al. (2001b) Ding et al. (2002), Lim et al. (2003), Govender et al. (2011), and Sichalwe et al. (2011).

The PEPT technique

Positron emission particle tracking (PEPT) is a Lagrangian, single-particle tracking technique in which the trajectory of a representative tracer particle is triangulated from the decay products of the positron-emitting radioisotope with which it is labelled (^{18}F in this work). It is an extension of the medical nuclear imaging technique positron emission tomography (PET) to the tracking of a single particle in a bulk, and is performed using the same equipment– a gamma camera– as is PET.

Both of these techniques rely on the detection of the products of positron annihilation. A positron emitted by the radioactive tracer particle annihilates with an electron in the surrounding material, producing a pair of back-to-back gamma rays that define a line of response (LoR) passing through (or very close to) the tracer. However, whereas PET produces a radiation density distribution by integrating a large number of detected LoRS over time, PEPT takes advantage of the *a priori* knowledge that the system of interest contains only one radiolabelled tracer particle to triangulate its position. Since the gammas are emitted uniformly in space, but all LoRs must pass through the tracer particle, detecting several LoRs allows the position of the tracer particle to be triangulated in space. Since each pair of gamma rays are detected coincidentally, each detection also has a time associated with it, and thus each triangulated tracer position can have an effective time assigned to it. The result is a series of Lagrangian tracer locations as a function of time.

In addition to true LoRs, the PET scanner also detects various types of spurious events, including false coincidences and scattered LoRs. Figure 2 shows true LoRs in blue, and spurious LoRS in red. In particular, the figure shows a false coincidence arising from two unassociated LoRs (dashed red) and the spurious LoR arising from a scattered gamma ray. To exclude spurious events such as these, Parker et al. (1993) developed a triangulation scheme that iteratively rejects the least good LoRs until a stopping criterion, such as spatial resolution, is met. While more sophisticated triangulation schemes– such as that of Bickell et al. (2012)– exist, the Parker routine is used here for simplicity.

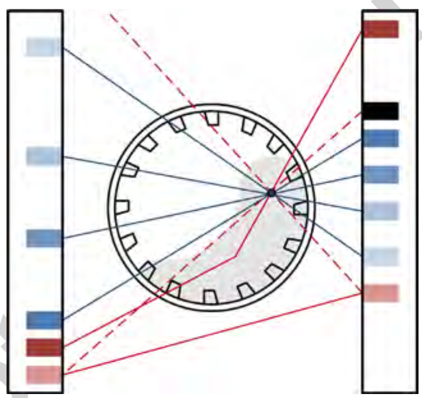

Figure 2: A 2D illustration of a realistic dataset consisting of both true (blue lines) and spurious events (red lines).

Figure 3 shows the University of Birmingham's ADAC Forte gamma camera. It is described in detail by Parker et al. (2002). In the field of view of the camera is the experimental rotating drum used for this work. It has an internal diameter of 300 mm and length of 270 mm, and is fitted with 20 lifter bars to increase the apparent friction between the drum and the granular bed.

Figure 3: The experimental rotating drum in the field of view of the Birmingham ADAC Forte gamma camera.

Lagrangian-to-Eulerian particle tracking

Although the trajectories of a tracer particle moving in a bulk of similar particles can be of interest, it is often more informative to employ the ergodic assumption and to thus convert trajectory data in the Lagrangian reference frame of the tracer into the fixed Eulerian reference frame of the system. The ergodic assumption can be stated as follows: Over a sufficiently long time, the time spent by a particle in some region of the phase space of microstates corresponding to a fixed macrostate of a system is proportional to the volume of that region of the phase space. That is, since the likelihood of a particle being in some microstate at a given time is proportional, and often assumed identical, to the likelihood of it being in that state at all, over a sufficiently long time a tracked particle will visit all possible combinations of position, momentum and so on with the probability of that microstate's instantiation.

Thus, given sufficiently many Lagrangian experiments performed on an ergodic system, it is possible to aggregate the recovered trajectories and sample them at fixed points in space to obtain a flow field in the Eulerian reference frame. In general, there is no way to determine *a priori* how many experiments need be performed, and for how long, to sample the entire phase space– for very asymmetric phase spaces, it may be practically impossible to do so– and so a pragmatic cut-off must be decided on. It may be possible, however, to measure some bulk property of the system that is also calculable from the accumulated trajectories in Eulerian form, and to use the convergence of the measured and calculated values as a guide. For our system of interest, the rotating drum, we use the convergence of the measured and calculated power drawn by the drum (Bbosa et al., 2011) as an ergodic criterion.

If the system of interest is in, or is sufficiently close to, steady state then it should be possible to obtain an Eulerian picture by combining (in some way) sufficient repetitions of a Lagrangian experiment as to completely sample every microstate of that system's phase space. If the system of interest is both steady-state and periodic, however, then a single, sufficiently long experiment could meet this requirement. Systems must at least meet the steady-state condition to be said to be *ergodic*.

The rotating drum experiments performed for this work are in steady state, and are performed for long enough to meet our chosen ergodic criterion, for their calculated and measured power draw to converge. Thus we are able to convert Lagrangian tracer particle trajectories into Eulerian flow fields via a procedure called residence time binning.

Residence time binning

Consider the illustrative trajectory shown in Figure 4a. It consists of a series of sample points along a path in 2D space, shown here as a dashed line. This sample trajectory is approximated by fitting a series of interpolating polynomials, as a function of time, to the sample points. Separate polynomials are fitted for each dimension– x, y and z– for a moving window of three tracer particle locations, corresponding to the span of a second order Lagrange polynomial. Thus, a trajectory consisting of N tracer locations will be approximated by $3\,(N-2)$ polynomials of the form $s_j(t) = p_j t^2 - q_j t + r_j$, where s is the generalised spatial coordinate, t is time, and the coefficient subscript j refers to the moving time interval for which the polynomial is defined. These piecewise approximations to the sample trajectory thus provide not only a means of estimating the tracer particle's position, but also– by taking their time derivative– its instantaneous kinematics, at any given time.

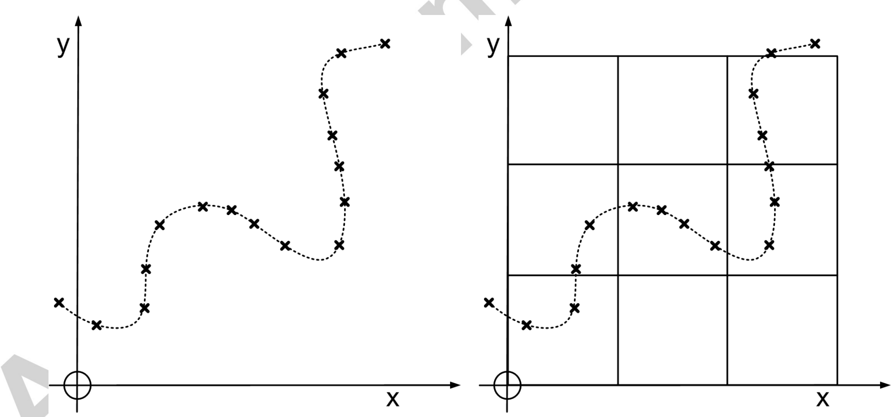

(a) 2D trajectory **(b)** Superimposed grid

Figure 4: An illustrative trajectory in 2D space without (left) and with (right) a binning grid superimposed.

The first step in recasting this now-continuous trajectory as an Eulerian flow field is to discretise the space into sample volumes (or voxels), as shown schematically in figure 4b. For clarity, the binning procedure is illustrated in 2D but, in practice, it is performed in 3D. These voxels represent the resolution of the flow field that will result from the binning procedure, and their minimum size is determined with reference to both the resolution of the imaging technique, and the chosen ergodic criterion. In this work, the voxels were cubic, and had a side length of approximately 2 mm.

The first Eulerian field of interest is the probability density, the likelihood that a particle of the sort represented by the tracer particle will be at any given location at any given time. By the ergodic assumption, this is the same as the residence time distribution (RTD). That is, the length of time spent by the tracer particle in each voxel is proportional to the likelihood of such a particle being in that voxel at any instant. The RTD of a tracer particle is obtained from its Lagrangian trajectory as follows.

Once the grid has been assigned, the sample points are replaced by the sample trajectory, defined in terms of the piecewise interpolating polynomials above. These interpolating polynomials can be inverted and solved for the boundaries of the voxels to determine the times at which the tracer particle entered and left each voxel, as illustrated in figure 5a. These times bound the time interval spent by the tracer in each voxel, as illustrated in figure 5b. Of course, the trajectory may pass through the same voxel many times, and so each voxel will contain a sum of all of the intervals that the tracer spent inside it. The more likely that the tracer will be in a given voxel at any time, the more times it will pass through that voxel, and the longer it will spend in that voxel, as per the ergodic assumption. Hence the raw RTD is proportional to the probability density. Finally, to obtain the actual probability density distribution, the raw RTD is normalised to the total time that the tracer was tracked for. From now on, the RTD will refer to the normalised (and not the raw) residence time distribution.

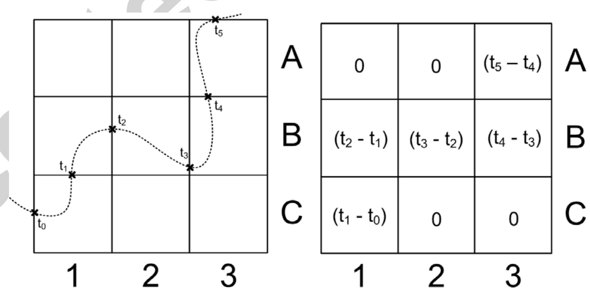

(a) Bin crossing times **(b)** Residence times

Figure 5: The residence time binning procedure: calculating bin boundary crossing times (left) and thus bin residence times (right).

The RTD can be interpreted as the most likely instantaneous distribution of material of the class being tracked in the system. It is thus directly useful as a measure of the shape of a granular bed, and can be used to assess whether bulk behaviours such as segregation or deadzones are arising. It can also be converted to a mass or solidicity distribution simply by multiplying it by the total mass or volume of the class of particles represented by the tracer respectively (Wildman et al., 2000).

The procedure for obtaining the RTD also facilitates that for obtaining the kinematics of the system. In particular, once the times that the tracer particle entered (t_i) and exited (t_f) a voxel on a transit j have been obtained, the average s-velocity of the tracer on that transit can be written as:

$$\bar{v}_{s,j} = \frac{\int_{t_i}^{t_f} v_s(t)dt}{\int_{t_i}^{t_f} dt} = \frac{s(t_f) - s(t_i)}{\Delta t_j} \tag{4}$$

where $s(t)$ is the relevant piecewise polynomial as defined above, $v_s(t) = \frac{ds(t)}{dt}$ and $\Delta t = t_f - t_i$. A similar procedure yields the average s-acceleration during transit j, where $a_s(t) = \frac{dv_s(t)}{dt} = \frac{d^2s(t)}{dt^2}$.

A single, representative value of each kinematic quantity is assigned to each voxel based on a time-weighted average of the values determined for each transit by equation 4. This corrects for the variation in transit length due to different tracer trajectories through the voxel, and for outlier values. The time-weighted average s-velocity of the N transits of the tracer through a given voxel is:

$$\bar{v}_s = \frac{\sum_{j=1}^{N} \Delta t_j \bar{v}_{x,j}}{T} = \frac{\sum_{j=1}^{N} \{s_j(t_f) - s_j(t_i)\}}{T} \tag{5}$$

where $T = \sum_{j=1}^{N} \Delta t_j$ is the total time spent by the tracer particle in that voxel over all of its transits.

This procedure can be performed in each dimension to obtain the $\hat{x}$-, $\hat{y}$- and $\hat{z}$-velocity flow fields, and a similar procedure can be performed to obtain the acceleration flow fields, and thus the full kinematics of particles of the class represented by the tracer.

Once the grid of voxels has been chosen, and the residence time binning procedure undertaken, the result is a series of three-dimensional grids containing the basic kinematic flow fields of the tracer particle in the Eulerian reference frame of the system. These can be combined to produce absolute velocity flow fields, or acceleration in the xy-plane, for instance. They can be sampled to produce sections along, or summed or averaged to produce projections onto, planes of interest, and– using the positions of the centroids of each voxel relative to an appropriate origin– they can be expressed in a coordinate system more natural to the system under study.

For this work, the RTD is used directly to investigate the shape of the granular bed, and both a cylindrical and Cartesian reference frame are used for various velocity distributions. Furthermore, the 3D grids are sectioned to exclude the end effects in the rotating drum, and projected onto the transaxial or $xy-$planes as appropriate.

The behaviour of a granular bed in a rotating drum

The bulk and bed free surfaces

The surface of a dynamic granular bed undergoing cascading motion in a rotating drum assumes an S-shape (Rajchenbach, 1990; Nakagawa et al., 1993; Taberlet et al., 2006). As the rotational speed increases, more and more material is thrown into flight, and the curvature of the S-shaped surface of the bed becomes more and more pronounced, until the bed enters the cataracting regime.

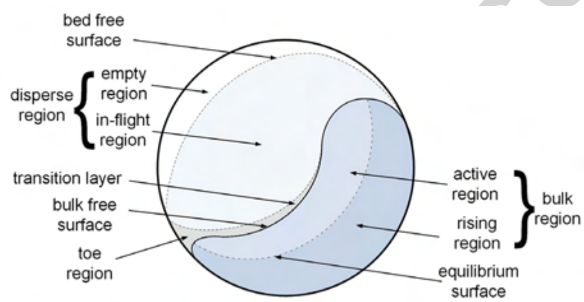

Figure 6: A schematic of the bed regions in a rotating drum.

Figure 6 shows a schematic of a typical granular bed undergoing cascading motion in a rotating drum. Under these conditions, the bed can be divided into two regions– the *bulk region*, and the *disperse region*. The bulk region is defined as that part of the granular bed consisting of particles in continuous contact with other particles in the bulk. The disperse region is so dilute that its constituent particles hardly interact with each other, except through collisions. Between the bulk and disperse regions is a *transition layer* in which particles are likely to collide with each other and with the bulk, but are still too dilute to be considered part of the bulk. This is most pronounced in the *toe region*, which is the most chaotic part of the bed, and the site of reincorporation of material from the disperse into the bulk region.

The disperse region also consists of two, easily-identifiable regions– the *empty region* and the *in-flight region*. The empty region is the area of the drum into which no material is ever thrown free of the bulk of the bed. The remainder is the in-flight region. The free surfaces that divide the bulk from the in-flight region, and the in-flight from the empty region, are called the *bulk free surface* and the *bed free surface* respectively. They can be identified from end-window filming, for example by Rogovin and Herbst (1989); from X-ray tracking, for example by Powell and Nurick (1996a); from computational discrete element models, for example by Powell and McBride (2004); or from PEPT data.

For this work, free surfaces were extracted from PEPT data by applying a closed-loop *Canny* edge detection routine (Canny, 1986) to transverse RTDs of the bed in motion. To deal with internal gaps, particularly in the in-flight region, a *Laplacian of a Gaussian* smoothing filter was first applied to the RTDs. The ambiguity of the transition layer was removed by setting as the edge-detection threshold the solidicity at which spherical particles lose contact with each other. The result is a robust numerical routine for extracting the free surfaces of a dynamic granular bed from its transverse RTD.

The equilibrium surface and the centre of circulation

The bulk region of the bed can be further divided into two distinct regions- the *rising region* and the *active region*. The rising region of the bed is that part that moves upwards and displays quasi-rigid body motion about the centre of the drum (Morrell, 1992). The active region consists of material flowing downwards over the rising material under the influence of gravity, and thus has previously been called the *descending region* (Powell and McBride, 2004). However, in a bed undergoing cascading or cataracting motion, it– together with the toe region– is the site of important processes such as mixing and grinding, and so is here called the active region.

The surface that separates the active from the rising region, shown schematically in figure 6, is called the *equilibrium surface*. It is so-called because it divides material moving in opposite directions and so, by continuity considerations, must consist of a layer of material that has zero net velocity in the appropriate direction (Powell and Nurick, 1996a; Powell and McBride, 2004). Figure 7 shows three schematics of the Eulerian velocity fields in a typical rotating drum, from which can be extracted the equilibrium surface.

The shape of the bulk of the bed is such that in its upper part, the rising material is moving essentially upwards and the active material is moving essentially downwards. Figure 7a shows the *vertical equilibrium surface*, which divides the rising and descending material. However, in the lower part of the bulk, the rising material is actually moving rightwards, and the active (and disperse) material is moving leftwards. Figure 7b shows the *horizontal equilibrium surface*, which divides the material moving in opposite horizontal directions. The combined equilibrium surface, which divides the rising and active regions, is a superposition of the two, and is shown in figure 7c.

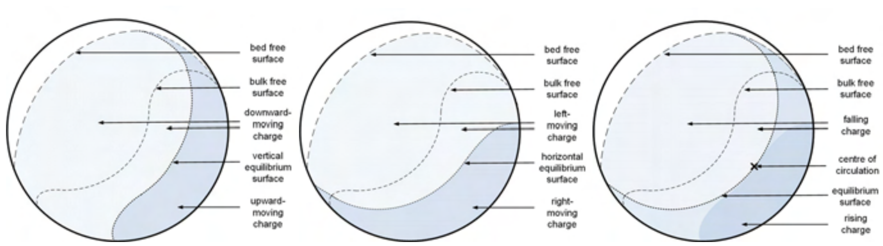

(a) Vertical equilibrium. **(b)** Horizontal equilibrium. **(c)** A superposition of equilibrium surfaces.

Figure 7: Schematics of the dynamic bed in a rotating drum showing the upward- and downward-moving (left), and leftward- and rightward-moving (middle) material separated by equilibrium surfaces, and the combined (right) equilibrium surface.

The point (or curve in three dimensions) through which the two equilibrium surfaces pass, as shown in figure 7c, is called the *centre of circulation* (CoC). Since it is the intersection of the horizontal and vertical velocity surfaces, it has zero velocity in both directions; it is the stationary point about which the bed revolves. In general, the CoC is not the same as the centre of mass of the bed, which is calculable from the RTD by assigned each bin the position of its centroid and a mass based on its normalised residence time.

The head, shoulders and toes

Although the free surfaces of the granular bed are a good indicator of the type of motion occuring in a rotating drum, it is often more convenient to compare different regimes by comparing so-called scalar indicators. Powell and McBride (2004) define four of these- the head, shoulder, bulk toe and impact toe of the charge. We adapt and extend these to obtain the bed features shown schematically in figure 8.

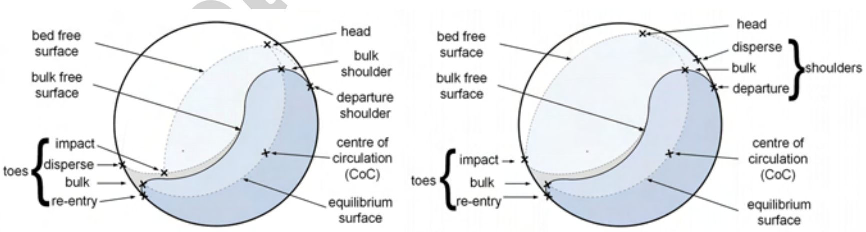

(a) Moderate rotational speed. **(b)** High rotational speed.

Figure 8: Schematics of the bed features in a rotating drum.

The *head* of the bed is the highest point attained by the outermost layer of in-flight material. It is obtainable from the RTD in one of two ways, depending on whether or not there is material in the in-flight region of bed. That is, if there is no material in the in-flight region, as happens at low speeds, the head is the intersection of the equilibrium surface and the bed free surface; if there is material in the in-flight region, the head is the intersection of the equilibrium surface and the bed free surface.

Powell and McBride (2004) define the shoulder of the bed as the point at which material leaves, and the toes as the highest points at which bulk and in-flight material strikes, the drum wall. We replace these with a series of toes and shoulders to reflect the greater range of bed behaviours that are possible within the cataracting and cascading modes.

We define the *departure shoulder* as the point at which material in the bulk of the bed leaves the drum wall, and define the *re-entry toe* as the point at which material from the active and bulk regions impact the drum wall. They are obtainable as the upper and lower intersections of the bulk free surface and the drum wall, respectively. Similarly, we define a *disperse shoulder* and *disperse toe* as the points at which material in the in-flight region leaves and regains contact with the drum wall. These are obtainable as the upper and lower intersections of the bed free surface and the drum wall, respectively.

At moderate speeds, the bed free surface can be broken down into two segments, as shown in figure 8a. The lower part consists of the upper boundary of the transition layer. The intersection of this part of the bed free surface and the drum wall is the disperse toe. The area between the disperse and re-entry toes is called the *toe region*, as shown in figure 6. The upper part of the bed free surface consists of the parabolic arc of the outermost material in the in-flight region. The *impact toe* is the point at which this parabolic trajectory ends. Thus the impact toe is defined as the lower intersection of the upper part of the bed free surface and the bulk free surface. However, at high rotational speeds, the in-flight material impacts directly on the drum wall, as shown in figure 8b, and the impact toe is defined as the lower intersection between the bed free surface, which consists then of only one segment, and the drum wall.

Finally, we introduce two new features; we define the *bulk shoulder* as the upper intersection of the bulk free surface and the equilibrium surface, and the *bulk toe* as the lower one. These, like the head, are turning points in the bed motion.

Not all of these bed features will exist at all drum rotational speeds, as shown in figure 8. As discussed before, at low speeds, there will be no material in the in-flight region, and so the bed and bulk free surfaces will coincide. In this case, the impact toe will not exist, the head will coincide with the bulk shoulder, and the disperse toe will coincide with the re-entry toe. Thus, neither the transition, nor the toe regions will exist in such a bed.

At moderate speeds, as shown in figure 8a, there is material in the in-flight region, but it is not thrown so far as to impact directly on the drum wall. In this case, the disperse and bulk shoulders may coincide, and the impact toe will be at a small angular and radial position than the bulk and disperse toes.

In this case, the disperse region will contain not only the in-flight and empty regions, but also parts of the transition and toe regions.

At high speeds, as shown in figure 8b, material in the in-flight region impacts directly on the drum wall, and so the disperse and impact toes coincide. Furthermore, the transition and toe regions are subsumed in the in-flight region of the bed.

At very high speeds, not shown in figure 8, the outermost layers may never leave the drum wall, as the motion begins to transition to centrifuging. In this case, the head of the bed is the highest point in the drum, and neither the impact toe nor disperse departure shoulder exist, although the bulk departure shoulder may still. Thus, neither the toe nor the empty regions exist at very high rotational speeds.

The effect of rotation speed on bed features

In this section we apply the characterisation routines described above to a mono-disperse bed of 5 mm glass beads in a 300 mm-diameter drum rotated at 50%, 60% and 75% of its critical speed. The drum has an internal length of 270 mm, and was filled to a load fraction of 31.25%.

The shape of the bed and the free surfaces

Figure 9 shows the transverse RTDs of the dynamic bed under these conditions. Below them is the scale used for all subsequent RTDs in this paper, with warmer colours signifying longer residence times, and cooler colours shorter ones.

Applying the edge detection routines described above to the dynamic beds shown in figure 9 allows them to be divided into their bulk, in-flight and empty regions. In particular, the dashed white lines in figure 10a show their bulk free surfaces, which become more and more S-shaped with increasing rotational speed.

Fitting a general logistic to these bulk free surfaces, as shown in figure 10b, simplifies the subsequent procedure of dividing the bed into its bulk and disperse regions for further analysis. For instance, the centres of mass (CoMs) of the entire bed and of only the bulk of the bed, at different rotational speeds, are given in table 1. Here, and for subsequent angular measures, angular position is measured in degrees from the right-hand half of the horizontal line through the centre of the drum. The radial position is measured, as usual, from the centre of the drum.

From table 1a, it can be seen that the CoM of the full bed moves upwards and inwards with increasing rotational speed– that is, towards the centre of the drum– as more material is thrown into the in-flight region. At the same time, the CoM of the bulk region moves upwards as the bulk elongates, but

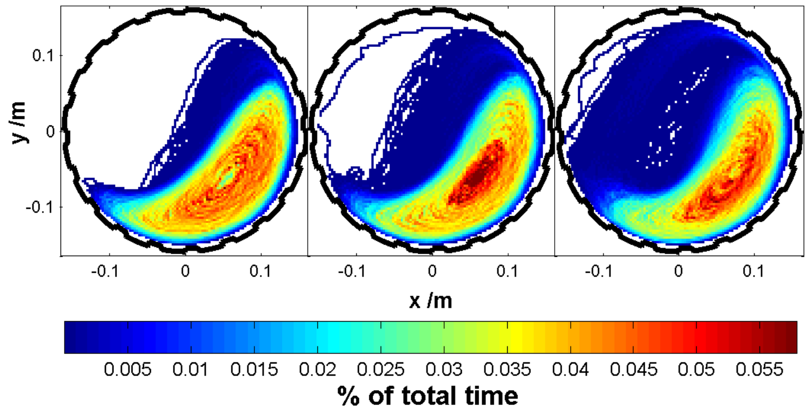

Figure 9: The residence time distributions of a 5 mm tracer particle in a 300 mm-diameter drum with a load fraction of 31.25%, rotated at 50% (left), 60% (middle) and 75% (right) of its critical speed.

Rot. speed / $\%v_{crit}$	Full bed θ / °	Full bed r /m	Bulk θ / °	Bulk r /m
50	-30.2	0.080	-46.7	0.084
60	-28.7	0.079	-43.9	0.085
75	-27.1	0.074	-42.2	0.085

(a) Centres of mass

Rot. speed / $\%v_{crit}$	In-flight mass fraction	Bed volume fraction
50	0.040	0.445
60	0.052	0.554
75	0.078	0.697

(b) Measures of mass distribution

Table 1: Angular and radial positions of the centre of mass of the bulk and full bed, the fraction of material in-flight, and the fraction of the drum volume occupied by charge for various rotational speeds.

stays roughly at the same radial distance from the centre of the drum. This is because the large increase in *bed volume*– the volume of the drum with a non-zero residence time– from $\sim 45\%$ to $\sim 70\%$ is due only to a very small mass fraction– $\sim 4\%$ of the total mass of the bed, as shown in table 1b.

Scalar measures of the bed shape

Once the equilibrium surfaces have been recovered from the RTDs by edge-detection, the shoulders and toes of the bed can be obtained from their intersection with the drum. Table 2 shows these intersections for the RTDs shown in figure 9.

Here, the angular compression of bulk of the bed is captured by the combination of a relatively small increase in the angular position of its departure shoulder with increasing speed, and a relatively large increase in the angular position of its re-entry toe. Some of this is due to the development of a dense central region

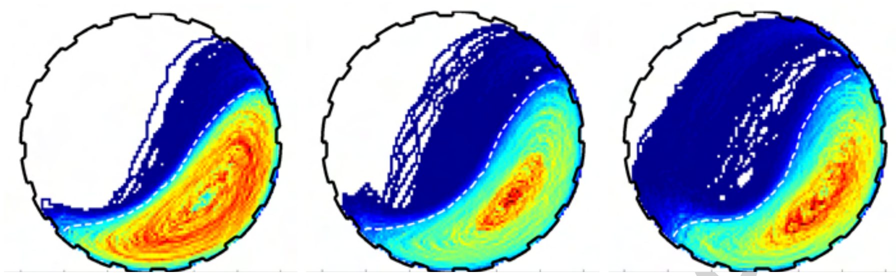

(a) Edge-detected bulk free surface

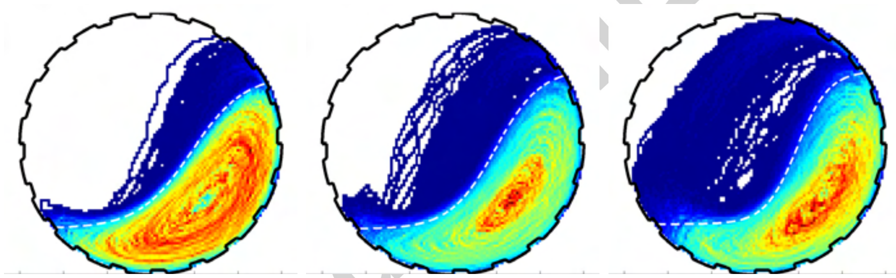

(b) Best fit general logistics

Figure 10: Edge-detected equilibrium surfaces (top), and their general logistic approximations(bottom), for the bed in a drum rotated at 50% (left), 60% (middle) and 75% (right) of its critical speed.

Speed ($\%v_{crit}$)	**Shoulder** (θ /°) **Departure**	**Disperse**	**Toe** (θ /°) **Re-entry**	**Disperse**	**Impact**
50	23.6	47.3	-153.4	-154.1	-121.5
60	27.3	50.8	-144.1	-157.9	-130.6
75	28.7	69.7	-135.0	-167.1	-167.1

Table 2: Angular positions of the departure and disperse shoulders; and re-entry, disperse and impact toes of a mono-disperse bed of 5 mm glass beads in a 300 mm-diameter drum with a load fraction of 31.25%, rotated at various speeds.

of the bed, but it also reflects the increasing amount of material in the in-flight, transition and toe regions.

As the rotational speed of the drum increases, more and more material enters the in-flight region as it is carried out of the bulk along the surface of the drum, leading to the increasing angular position of the disperse shoulder, and to the increasing angular separation of the disperse and departure shoulders.

As more charge enters the disperse region, a chaotic transition and toe region develops. The development of the toe region is evidenced by the increasing angular separation between the re-entry and disperse toes with increasing speed. At very low speeds, there is essentially no toe region, and at very high speeds, it is significant in size.

Finally, from table 2, it is possible to draw some inferences about the nature of the toe region from the angular position of the impact toe. At 50% and 60% of critical speed, the in-flight material lands on the surface of the bulk, as evidenced by having impact toes below their re-entry toes. In the 50% case, the small amount of material in the in-flight region lands so high up on the bulk, that it is effectively flowing with the active region by the time it reaches the re-entry toe, resulting in essentially no toe region. In the 60% case, there is more material landing lower down the bulk, leading to a small but chaotic toe region. In the 75% case, the highest material in the in-flight region impacts directly on the drum wall, and so there is no difference between the disperse and impact toes. The result is a large and chaotic toe region.

Rot. speed / $\%v_{crit}$	**Head** θ /°	h / % max
50	62.7	90.4
60	72.9	94.2
75	81.9	97.1

Table 3: The angular and normalised vertical positions of the highest point reached by a mono-disperse bed of 5 mm glass beads in a 300 mm-diameter drum with a load fraction of 31.25%, rotated at various speeds.

Also from the bed free surface, which separates the in-flight from the empty regions, it is possible to obtain the head of the bed. Table 3 shows the angular position of the head with increasing rotational speed, as well as its vertical height above the lowest point of the drum, normalised to the drum diameter. This is of interest because it determines the maximum potential energy available to a particle in the bed. As expected, the position of the head approaches the highest point in the drum as more and more material is thrown into the in-flight region. At lower speeds than shown here, the head of the bed would coincide with its bulk shoulder.

The motion of the bed and the equilibrium surface

Figure 11 shows the $\hat{x}$- and $\hat{y}$-velocity distributions corresponding to the RTDs shown in figure 9. Below them is the scale used for all subsequent velocity distributions in this paper, with warmer colours signifying large positive speeds, and cooler colours large negative ones.

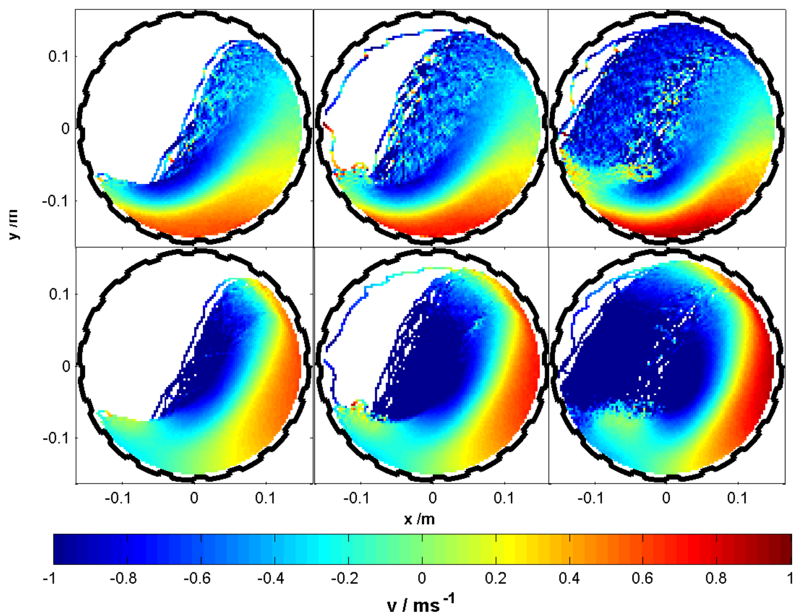

Figure 11: Time-weighted $\hat{x}$- (top) and $\hat{y}$-velocity (bottom) distributions for the bed in a drum rotated at 50% (left), 60% (middle) and 75% (right) of its critical speed.

The velocity distributions in figure 11 clearly demonstrate the separation of leftward- and rightward-moving material, and upward- and downward-moving material by surfaces of zero velocity, as shown schematically in figure 7. These zero-velocity surfaces are obtained quantitatively from the zero-velocity *equilibrium points* in each direction, as follows.

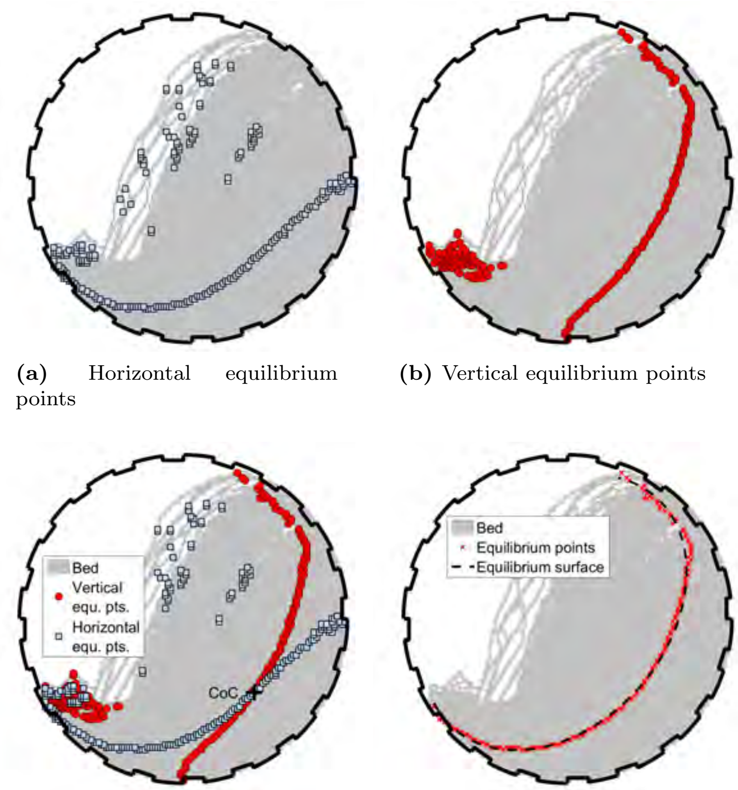

(a) Horizontal equilibrium points **(b)** Vertical equilibrium points

(c) Combined equilibrium points **(d)** Equilibrium surface

Figure 12: The horizontal and vertical equilibrium points of the velocity distributions of a granular bed in a drum rotated at 60% of its critical speed, separately (above), combined (below left), and with the equilibrium surface superimposed (below right).

The top row of figure 12 shows the equilibrium points in the transverse $\hat{x}$- and $\hat{y}$-velocity distributions of the bed in a drum rotated at 60% of its critical speed, that is, of the distributions in the central column of figure 11. Figure 12c shows the two equilibrium surfaces defined by these equilibrium points intersecting at the centre of circulation (CoC) of the bed, and figure 12d shows the equilibrium points that make up the final equilibrium surface with an elliptical arc fitted to them.

Figure 13 shows the RTDs of the granular bed in the drum rotated at the three speeds. Superimposed thereon are not only approximations to the bulk free surfaces shown in figure 10, but also to the equilibrium surfaces of the bed in motion. As with the general logistics fitted to the bulk free surfaces before, the elliptical arcs fitted to the equilibrium surfaces do not represent an underlying model, but are adopted merely to simplify further analysis.

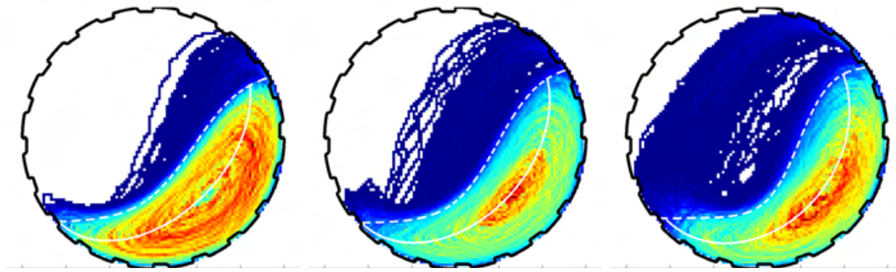

Figure 13: General logistic and elliptic approximations to the bulk free (dashed white lines) and equilibrium (solid white lines) surfaces of a granular bed in a drum rotated at 50% (left), 60% (middle) and 75% (right) of its critical speed.

In this case, the equilibrium surface divides the bulk of the bed into its rising and active regions, allowing a more quantitative discussion of the behaviour of the bulk of the bed. For instance, the total mass and volume fractions can be obtained for these two regions, as they were for the bulk and disperse regions in table 1b. From these, the density of the bed in the rising and active regions, shown in table 4 normalised to that of close-packed glass spheres, can be calculated.

Rot. speed / $\%v_{crit}$	**Relative density** In-flight	Active	Rising
50	0.091	0.953	0.993
60	0.069	0.931	0.989
75	0.066	0.855	0.969

Table 4: The density of the bed in the rising, active and in-flight regions, normalised to the density of close-packed glass spheres.

The change in densities with increasing rotational speed confirm that– since it is able to dilate more or less freely, constrained only by the very dilute disperse region– the active region of the bed fluidises more quickly than the rising region, which continues to act as a more or less solid body as the rotational speed increases. Furthermore, the relatively density of the in-flight material in the slowest case reflects the fact that the material in the transition and toe regions are effectively just a dilute part of the active region.

Scalar measures of the bed motion

As well as dividing the bulk region of the bed into its rising and active regions, the equilibrium surface can be used to obtain the centre of circulation (CoC) of the bed, and its bulk toe and shoulder. The CoC is obtained as part of the procedure for obtaining the equilibrium surface, as shown in figure 12d, while the bulk toe and shoulder are the upper and lower intersections of the equilibrium with the bulk free surface.

The re-entry toe and departure shoulder, as given in table 2, mark the beginning and end of a special type of motion: circular motion of the bed with the drum, and the disperse shoulder and toe mark the beginning and end of the motion of material in free fall. In contrast, the bulk shoulder and toe do not mark the beginning or end of any type of motion, but rather turning points in the motion of the bed. In this respect, they are like the head of the bed, which marks a turning point in the free fall motion of material in the in-flight region. In fact, all of the turning points of the bed motion are joined by the equilibrium surface– the head can be defined as the intersection of the equilibrium and bed free surfaces– and so can be considered special equilibrium points. The CoC is also a special equilibrium point– it is the only stationary point in the bed. Table 5 shows the radial and angular positions of these three features at various drum rotational speeds.

Rot. speed	**CoC**		**Bulk shoulder**		**Bulk toe**	
/ $\%v_{crit}$	θ / °	**r /m**	θ / °	**r /m**	θ / °	**r /m**
50	-52.6	0.091	28.7	0.127	-149.0	0.141
60	-47.7	0.093	32.2	0.126	-151.9	0.142
75	-44.1	0.098	36.3	0.124	-153.4	0.135

Table 5: Angular and radial positions of the CoC, and bulk shoulder and toe of the bed in a drum rotated at various speeds.

The bulk shoulder and toe give an indication of the extent of the bulk region. Table 5 shows the gradual angular elongation of the bulk with increasing speed, with slightly more of an effect in the position of the shoulder than the toe. It also shows the gradual radial thickening of the bulk at the toe and shoulder with increasing speed, with a significant thickening of the toe region at high speeds. At the same time, the radial position of the CoC increases, reflecting the increasing S-shape of the bulk. The CoC also moves higher up in the bulk, relative to both the bulk toe and shoulder, as the bulk itself moves up in the drum.

The thinning of the central part of the rising region, suggested by the movement

Rot. speed / $\%v_{crit}$	**Active** \m	**Rising** \m	**Relative thickness**
50	0.046	0.059	0.771
60	0.045	0.057	0.799
75	0.051	0.052	0.989

Table 6: Relative thicknesses of the rising and active regions of the bed in a drum rotated at various speeds.

of the CoC outwards with increasing mill speed, is more clearly captured in the ratio of the thickness of the rising and active regions along a line passing through both the centre of the drum, and the CoC of the bed. Table 6 contains these ratios, which far better illustrate the significant change in bed behaviour between 60% and 75% of critical speed, evident from a visual inspection of figure 9.

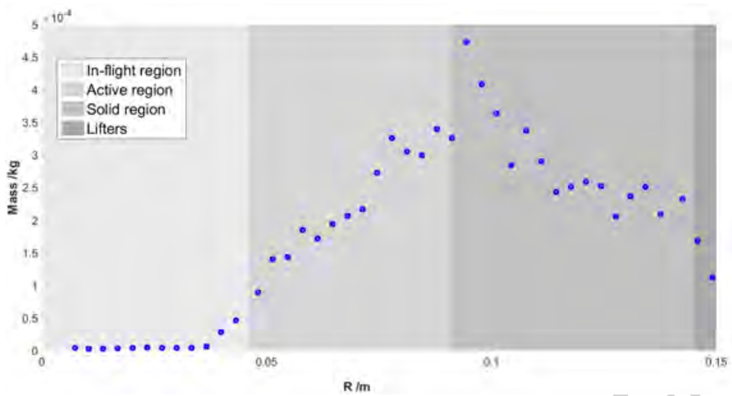

Figure 14: The mass profile of the dynamic granular bed in a drum rotated at 60% of its critical speed, sampled along the line passing through the centre of the drum and the centre of circulation of the bed.

Any line passing through the CoC of the bed must have the following property: the flux of material passing through it must be zero. In addition, any line passing through both the centre of the drum, and the CoC of the bed must pass through all of the distinct regions of the bed shown in figure 6, except the chaotic toe region. This makes such a line an ideal one along which to sample Eulerian distributions to produce graphs such as the mass profile shown in figure 14.

Figure 14 shows a mass profile obtained by selecting voxels from the total mass-weighted RTD of the bed in a drum rotated at 60% of its critical speed along the line defined above. It provides a more detailed idea of the density in various regions than does table 4. For ease of interpretation, the mass curve is plotted on top of grey blocks representing the empty, in-flight, active and rising regions (from left to right in the image). From this, the dense core visible in the central graph in figure 9 is evident as a peak in the mass profile. Also, the ambiguity of the transition zone is illustrated by the continuous mass curve between the active and in-flight regions.

Conclusions

In this paper we have dissected the dynamic bed of granular material in a rotating drum, and shown how the shape and behaviour of such a bed changes with increasing rotational speed. In so-doing, we have defined various surfaces that divide the bed into distinct regions, and obtained various bed features from the intersections of these surfaces. We have described the procedure for converting Lagrangian data of the type obtainable from PEPT into Eulerian flow fields more amenable to investigation and modelling of bed behaviour, and the procedures for obtaining the surfaces and features described below from such Eulerian flow fields. Finally, we have illustrated their application with real data, and gained an insight into how the behaviour of a dynamic granular bed changes with increasing rotational speed of the drum that it is in.

In particular, we have divided the bed into the dense *bulk region* consisting of particles in continuous contact with each other, and the complementary dilute *disperse region*, separated by an intermediate-density *transition region* consisting of the most highly-fluidised material at the surface of the bulk region, and material from the disperse region re-joining the bulk. We have divided the bulk into the *rising region*, consisting of densely-packed particles rising in solid-body motion with the drum, and the *active region*, consisting of dilated material flowing downwards over the rising region, and the disperse region into the *in-flight region*, into which material is thrown by the action of the rotating drum, and the *empty region*, which the material of the bed never reaches. Further, we have identified the more or less chaotic *toe region* at the base of the bulk; the confluence of material leaving the in-flight, transition and active regions, and re-entering the rising region.

We have made this division of the bed by defining the *bed free surface*, which divides the in-flight region from the empty region; the *bulk free surface*, which divides the bulk from the disperse region of the bed; and the *equilibrium surface*, which divides the rising, en-masse material from the falling material in the bed and, in the bulk, separates the rising and active regions.

Finally, we have defined various bed features as the intersection of these surfaces with each other, and with the drum. Due to the changing shape and behaviour of the bed with increasing drum rotational speed, not all of these are defined at all speeds, but we attempt to deal with redundancies. For instance, we define the *head* of the bed as the intersection of the equilibrium and bed free surfaces unless there is no material in the in-flight region, in which case, the bed and bulk free surfaces are degenerate, and the head coincides with the *bulk shoulder*. Similarly, we define the *impact toe* and *disperse shoulder* as the intersection of the bed free surface and the drum, unless either there is no material in flight, and the disperse shoulder coincides with the *departure shoulder*, or the in-flight material strikes the surface of the bulk and not the drum, in which case we define a *disperse toe* as the upper extent of the *toe region*. And so on.

References

Bbosa, L.S., Govender, I., Mainza, A.N., Powell, M.S., 2011. Power draw estimations in experimental tumbling mills using pept. Minerals Engineering

24, 319–324.

Bickell, M., Buffler, A., Govender, I., Parker, D.J., 2012. A new line density tracking algorithm for pept and its application to multiple tracers. Nuclear Instruments and Methods in Physics Research Section A - Accelerators, Spectrometers, Detectors and Associated Equipment 682, 36–41.

Boateng, A.A., Barr, P.V., 1996. Modelling of particle mixing and segregation in the transverse plane of a rotary kiln. Chemical Engineering Science 51, 4167–4181.

Canny, J., 1986. A computational approach to edge detection. IEEE Transactions on Pattern Analysis and Machine Intelligence PAMI-8, 679–698.

Ding, Y.L., Forster, R., Seville, J.P.K., Parker, D.J., 2002. Granular motion in rotating drums: bed turnover time and slumpingrolling transition. Powder Technology 124, 1827.

Ding, Y.L., Forster, R.N., Seville, J.P.K., Parker, D.J., 2001a. Scaling relationships for rotating drums. Chemical Engineering Science 56, 37373750.

Ding, Y.L., Seville, J.P.K., Forster, R., Parker, D.J., 2001b. Solids motion in rolling mode rotating drums operated at low to medium rotational speeds. Chemical Engineering Science 56, 1769–1780.

Govender, I., Mangesana, N., Mainza, A.N., Franzidis, J.P., 2011. Measurement of shear rates in a laboratory tumbling mill. Minerals Engineering 24, 225–229.

Govender, I., Powell, M.S., Nurick, G.N., 2001. 3D particle tracking: A rigorous technique for verifying DEM. Minerals Engineering 14(10), 1329–1340.

Jain, N., Ottino, J.M., Lueptow, R.M., 2002. An experimental study of the flowing granular layer in a rotating tumbler. Physics of Fluids 14, 572–582.

Lim, S.Y., Davidson, J.F., Forster, R.N., Parker, D.J., Scott, D.M., Seville, J.P.K., 2003. Avalanching of granular material in a horizontal slowly rotating cylinder: Pept studies. Powder Technology 138, 25–30.

Mellmann, J., 2001. The transvers motion of solids in rotating cylinders- forms of motion and transition behaviour. Powder Technology 118, 251–270.

Morrell, S., 1992. Prediction of grinding-mill power. Transactions of the Institution of Mining and Metallurgy Section C: Mineral Processing Extraction and Metallurgy 101, C25–C32.

Nakagawa, M., Altobelli, S.A., Caprihan, A., Fukushima, E., Jeong, E.K., 1993. Non-invasive measurements of granular flows by magnetic resonance imaging. Experiments in Fluids 16(1), 54–60.

Parker, D.J., Broadbent, C.J., Fowles, P., Hawkesworth, M.R., McNeil, P., 1993. Positron emission particle tracking - a technique for studying flow within engineering equipment. Nuclear Instruments and Methods in Physics Research A 326, 592. Unread.

Parker, D.J., Forster, R.N., Fowles, P., Takhar, P.S., 2002. Positron emission particle tracking using the new birmingham positron camera. Nuclear Instruments and Methods in Physics Research A 477, 540–545.

Powell, M.S., McBride, A.T., 2004. A three-dimensional analysis of media motion and grinding regions in mills. Minerals Engineering 17, 1099–1109.

Powell, M.S., Nurick, G.N., 1996a. A study of charge motion in rotary mills part 1- extension of the theory. Minerals Engineering 9, 259–268.

Powell, M.S., Nurick, G.N., 1996b. A study of charge motion in rotary mills part 2- experimental work. Minerals Engineering 9, 343–350.

Rajchenbach, J., 1990. Flow in powders: From discrete avalanches to continuous regime. Physical Review Letters 65(18), 2221–2224.

Rogovin, Z., Herbst, J.A., 1989. Charge motion in a semi-autogeneous grinding mill. Minerals and Metallurgical Processing 6, 18–23.

Rose, H.E., Sullivan, R.M.E., 1957. A treatise on the Internal Mechanics of Ball, Tube and Rod mills. Constable, London.

Santomaso, A.C., Ding, Y.L., Lickiss, J.R., York, D.W., 2003. Investigation of the granular behaviour in a rotating drum operated over a wide range of rotational speed. Transactions of the Institute of Chemical Engineers 81, 936–945.

Sichalwe, K., Govender, I., Mainza, A.N., 2011. Characterising porosity of multi-component mixtures in rotary mills. Minerals Engineering 24, 276–281.

Taberlet, N., Richard, P., Hinch, E.J., 2006. S shape of a granular pile in a rotating drum. Physical Review E 73, 050301–1–4.

Tordesillas, A., Arber, D., 2005. Capturing the s in segregation: A simple model of flowing granular mixtures in rotating drums. International Journal of Mathematical Education in Science and Technology 36(8), 861–877.

Watanabe, H., 1999. Critical rotation speed for ball-milling. Powder Technology 104, 95–99.

Wildman, R.D., Huntley, J.M., Hansen, J.P., Parker, D.J., Allen, D.A., 2000. Single-particle motion in three-dimensional vibrofluidized granular beds. Physical Review E Volume 62, Number 3, 3826–3835.